High-performance Continuous Hydraulic Motor for MR Safe Robotic Teleoperation

Ziyang Dong, Ziyan Guo, Kit-Hang Lee, Ge Fang, Wai Lun Tang, Hing-Chiu Chang, Danny Tat Ming Chan and Ka-Wai Kwok, *Senior Member*, IEEE

***Abstract*—Magnetic resonance imaging (MRI)-guided intervention has drawn increasing attention over the last decade. It is accredited to the capability of monitoring any physiological change of soft tissue with the high-contrast MR images. This also gives rise to the demand for precise tele-manipulation of interventional instruments. However, there is still lack of choices of MR safe actuators that provide high-fidelity robot manipulation. In this paper, we present a three-cylinder hydraulic motor using rolling-diaphragm-sealed cylinders, which can provide continuous bidirectional rotation with unlimited range. Both kinematics and dynamics models of the presented motor were studied, which facilitate its overall design optimization and position/torque control. Motor performance, such as step response, frequency response, and accuracy, were experimentally evaluated. We also integrate the motor into our catheter robot prototype designed for intra-operative MRI-guided cardiac electrophysiology (EP), which can provide full-degree-of-freedom and precise manipulation of a standard EP catheter.**

***Index Terms*— Hydraulic actuators, medical robotics, MR safe robot, catheterization, robot-assisted intervention**

I. Introduction

MAGNETIC resonance imaging (MRI) is well-known for its superior capabilities in providing non-invasive, non-ionizing radiation high-contrast images of soft tissues, and also in monitoring the temperature changes during thermal therapy procedures [1]. These advantages prompted the adoption of MRI guidance for interventions ranging from biopsy [2], thermal therapy for tumor ablation [3], drug delivery [4] to catheter-based procedures within cardiovascular system [5, 6]. However, precisely manipulating the instrument within the limited workspace of MRI bore still remains challenging. A number of research attempts [7, 8] have focused on developing tele-operated robotic platforms for the interventions, demonstrating enhanced accuracy and reduced procedural time under intra-operative (intra-op) MRI.

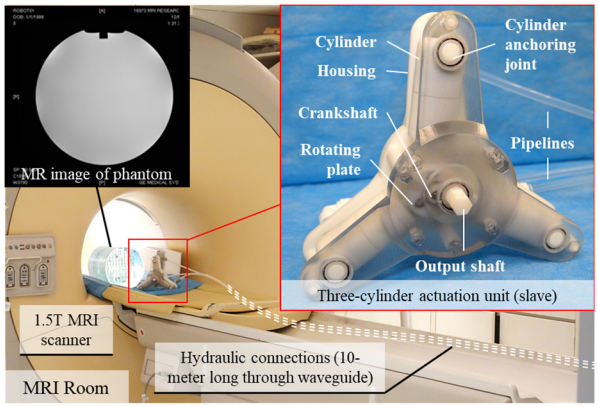

Fig. 1. Setup of the three-cylinder motor in the 1.5T MRI scanner. This MR safe motor is connected with three pipelines which transmit motion from the master unit in the control room. The MR image of an MRI phantom placed aside the actuator indicates the negligible EM interference.

The early MRI-guided robot was developed by Chinzei *et al.* [9] in brachytherapy of prostate cancer. The robot is actuated by piezoelectric motors, which make use of high-frequency current to excite precise stepping action. In order to minimize the EM interference, the motors have to be placed far away from the imaging region to manipulate the interventional tools. Recent studies (Su *et al.* [10]) also explore the use of tailor-made components to attenuate the EM interference. Much effort has also been made in designing the EM-shield enclosures, and also customizing the motor driver for low loss of SNR (2%) during their motor operation. Nevertheless, due to the fundamental working principle of stepping and friction driven, it is challenging to apply piezoelectric motor to procedures which require outstanding dynamic performance.

Inherently MR safe motors powered by fluid, e.g. pneumatic motors [11-13], have also been widely discussed. Stoivanici *et al.* [14] developed a robot for intra-op MRI-guided prostate biopsy, which was fully driven by pneumatic stepper motors. Groenhuis *et al.* [15] did various prototypes for breast biopsy. Their motor design is compact and seamlessly integrated with the robot for precise manipulation of a needle. However, other than biopsy, particularly in certain procedures demanding for prompt and responsive manipulation/navigation of instruments, e.g. electrophysiology (EP) catheterization in dynamic cardiovasculatures, the high compressibility of air will cause difficulties in handling the dynamics and also the mechanical transmission delay. Moreover, delicate handling of regulation valves and air dissipation is needed to avoid excessive noise

Manuscript received: September 10, 2018; Revised: December 17, 2018; Accepted January 24, 2019. This paper was recommended for publication by Editor Paolo Rocco upon evaluation of the Associate Editor and Reviewers' comments. This work is supported in parts by Signate Life Sciences (Hong Kong) Limited, the Croucher Foundation, the Research Grants Council (RGC) of Hong Kong (Ref. No. 27209151, No. 17227616, and No. 17202317).

Z. Dong, Z. Guo, K.H. Lee, G. Fang, W. L. Tang and K.W. Kwok are with Department of Mechanical Engineering, The University of Hong Kong, Hong Kong (corresponding author, Tel: +852-3917-2636; e-mail: kwokkw@hku.hk).

H.C. Chang is with Department of Diagnostic Radiology, The University of Hong Kong, Hong Kong.

D.T.M. Chan is with Department of Surgery, The Chinese University of Hong Kong, Hong Kong.

Digital Object Identifier (DOI): see top of this page.

and vibration, along with the acoustic noise existing from MRI scanner (~100dB), which may cause patient anxiety.

Therefore, hydraulic actuation using incompressible fluid (e.g. water, oil) as transmission media can offer much faster response and higher power density [16, 17]. However, conventional piston-cylinder paradigm often suffers from large Coulomb friction due to the tight O-ring sealing, which introduces substantial mechanical losses and nonlinearities to the control system. Whitney *et al.* [18] developed an efficient fluid transmission based on the rolling-diaphragm-sealed metallic cylinders, which can greatly reduce the mechanical friction. This concept has been adopted to our recent MRI-guided robotic catheterization platform [19] that is made of solely non-metallic materials. The system has demonstrated accurate and dexterous manipulation of EP catheter. However, the diaphragm can only be flipped inside out with a limited stroke (**Fig. 2a**), which is insufficient to navigate the full length required in EP. Although the effective stroke can be increased by gearing up the actuator, it will inevitably compromise the output torque and durability of non-metallic components.

This poses strong incentive to develop a novel integration method of these fluid transmissions, which is MR safe and capable of bi-directional rotation with infinite range and high payload. Such technique is expected to resolve many bottlenecks involved in teleoperating MRI-guided surgical apparatus. For example, high-intensity focused ultrasound (HIFU) thermal therapy under MRI is a noninvasive ablation approach, which currently still relies on manual positioning of a *heavy* ultrasound transducer array.

In this paper, with the aim to solve the unmet clinical needs for tele-operated, dexterous control of interventional tools under MRI, we propose an MR safe motor design capable of providing *unlimited* range of continuous bidirectional rotation (**Fig. 1**). These capabilities would be comparable to the conventional EM-motor for versatile applications even involving high payload manipulation. The key contributions of our work are listed below:

1) Design of a three-cylinder hydraulic motor for high-performance tele-operation of MRI-guided robotic interventions. It can achieve continuous bidirectional actuation with unlimited motion range. The motor can also be customized with more cylinders (>2) to provide higher output torque;

2) Dynamics modelling of the hydraulic actuation was studied for design optimization. Both positional and torque control can be applied;

3) Experimental validation of transmission step response, force transmission, frequency response and accuracy are conducted to ensure dexterous robotic actuation. The three-cylinder hydraulic motor has also been integrated into an MR safe robotic platform for cardiac catheterization, which is tested by a long-range navigation task.

II. Design of Diaphragm-based Hydraulic Transmission

Fig. 2a shows a pair of cylinders enabling action-and-reaction transmission via a long hydraulic tube (10-meter) that passes through the waveguide in between MRI and control room. Incompressible liquid, such as water or oil, is fully filled in the pipelines to ensure responsive, accurate power transmission in both directions. Considering the trade-off between pliability and stiffness of the tube for such long-distance transmission, semi-rigid nylon tubes with outer/inner diameter of Ø6/4 mm (DG-5431101, Daoguan Inc.) are selected. Radial expansion of these tubes under loading is minimal when the transmission liquid inside is pressurized. Key components in our current prototype, such as piston rods and cylindrical housings, are 3D-printed with polymer composites (VeroWhitePlus and VeroClear, Stratasys, US), ensuring the MR safety. To enhance the structural rigidity and robustness in production stage, alternative choices of MR safe materials with higher strength, e.g. polyethylenimine, polyoxymethylene, will be explored and adopted.

Each cylinder unit contains a rolling diaphragm (MCS2018M, FEFA Inc.) made of fabric-reinforced rubber for fluid sealing. The diaphragm can be flipped inside out, and roll

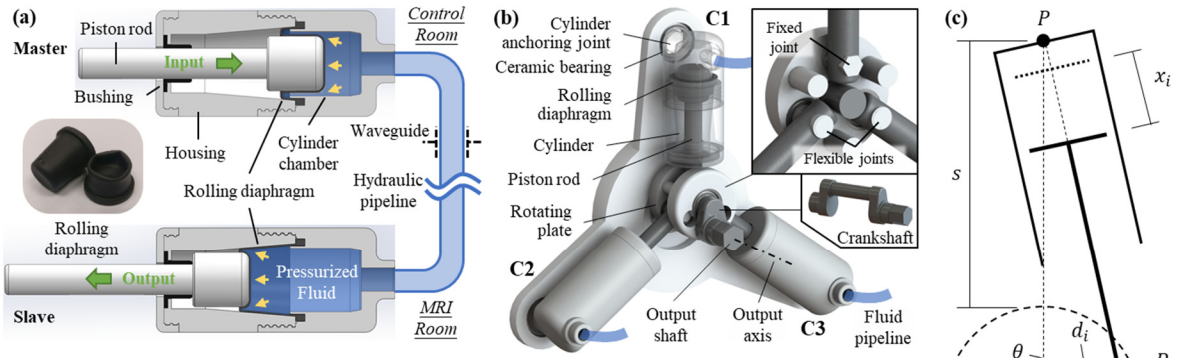

(d) Key Parameters of Three-cylinder Actuator

Parameter	Description	Parameter	Description
x_i	Piston displacement	r	Radius of rotating plate
s	Distance from point P to the nearest point on crankshaft trajectory	R	Radius of crankshaft
		θ	Angular position of the output shaft
d_i	Distance between the center line of the i^{th} piston rod and the rotation axis of output shaft	β	Angle between the piston rod and the direction of the rotating plate relative to the output axis

Fig. 2. (a) Pair of cylinders enabling MR safe power transmission through a long hydraulic tube via the waveguide in-between control room (master control side) and MRI suite (slave robot side). Rolling diaphragms are adopted to tightly sealed the fluid, and also to slide inside the cylinder with minimal friction. **(b)** 3D model showing the piston rods coupled with the output shaft by hinging a rotating plate and crankshaft; **(c)** Kinematics parameters denoted in a single cylinder, which are summarized in **(d)**.

over the piston rod to allow 35-mm stroke linear motion. Its working principle inherently averts the sliding friction between the seal and cylinder, which is a great concern in the conventional O-ring-sealed hydraulic transmission [18]. However, the transmission can only take place when the piston rod is pushed onto the diaphragm hat. Therefore, only one-to-one cylinders *cannot* conduct bidirectional transmission. In this light, the integration of multiple cylinders pairs is proposed to generate actuation in both directions. Our previous work demonstrated the *two*-cylinder configuration [19]. However, the short motion range is still far from satisfying requirements for high-precision and long-range navigation, e.g. for needle insertion (>100 mm [20]) or EP catheterization from femoral vein to heart chamber. To this end, fundamental change of cylinders configuration is proposed to resolve the unmet technical/clinical requirements.

A. Continuous actuation with three-cylinder configuration

Fig. 1 and **Fig. 2b** show the prototype and 3D model of the proposed MR safe motor, respectively. It integrates *three* hydraulic cylinders. This design is capable of bidirectional, continuous and torque-controllable rotatory actuation, in contrast to aforementioned stepper motors with pneumatic cylinders that only allow full-stroke movement [21]. Continuous motion is made possible by taking advantage of the rolling diaphragm seal, which enables precise control of displacement/force of each cylinder, even when connected through 10-meter hydraulic pipelines.

The output shaft of our motor is simultaneously driven by all cylinders, radially placed with 120° intervals. This design aims to avoid kinematics singularity, where no output torque can be generated regardless of how the cylinders are actuated. However, for fluid-driven cylinders that only allow for push motion, singularity becomes inevitable if only one or two cylinders are employed in a craft-shaft mechanism. This necessitates a minimum of three-cylinder design to enable smooth rotary motion. The allowable output torque could also be increased by employing additional cylinders.

B. Kinematics model

Kinematics of the three-cylinder configuration is derived based on the actuator geometry. Key kinematics parameters of a single cylinder are depicted in **Fig. 2d**. All the components, except for the rolling diaphragm, are considered as rigid bodies. Unique solution of each piston displacement, x_i, is obtainable, corresponding to an angular position θ of the output shaft. By applying Cosine Law for the triangle ΔOAP in **Fig. 2c**, the piston displacement of the cylinder C_1 can be calculated as:

$$x_1(\theta) = \sqrt{2R(R+s)(1-\cos\theta)+s^2} - s\,. \tag{1}$$

As the pistons are evenly placed in a circle, the i^{th} cylinder C_i has a phase difference $\varphi_i = (i-1)\cdot 2\pi/n$ compared with cylinder C_1 where n is the total number of cylinders and equals to 3 for the three-cylinder configuration. Therefore, the piston displacements of the cylinders can be derived by adding the phase difference to θ in **(1)**. Note that the misalignment is negligible for the installation of the rotating plate.

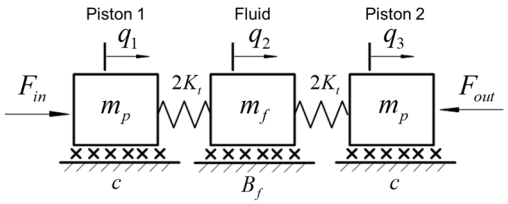

Fig. 3. Dynamics parameters of a single-pipeline transmission. Input force F_{in} is applied to move Piston 1 at constant velocity, with output force F_{out} equal to zero. The cross markers "×" denote the fluid damping.

C. Dynamics model

To identify the system properties and optimize the design parameters, we established the model of the integrated transmission system and carry out the validation, not only in simulation but also in the experimentation. Provided with the dynamics model of our proposed actuator, we can identify the key parameters that govern the system performance, hence defining a design guideline to fulfill various practical requirements and constraints.

The proposed transmission system adopts a master-slave design, with two sides connected by several hydrostatic transmission pipelines. The slave side is the three-cylinder actuation unit, while the master side comprises of the same number of cylinders individually driven by electric motors. The system dynamics model is derived in two sections, namely the slave actuation unit and the hydraulic transmission.

1) Dynamics modeling of slave actuation unit

Two assumptions are taken into account: **1)** all the components are rigid body, except for the rolling diaphragm and pipelines; **2)** friction at the joints is negligible. Each cylinder can only generate a unidirectional force, which comes from the fluid pressure in the pipeline. The output torque contributed by the i^{th} cylinder can then be described as $\tau_i = F_i \cdot d_i$, where F_i is the force provided by the cylinder and d_i is the offset between the center line of the i^{th} piston and the rotation axis of output shaft. From **Fig. 2c**, d_i can be calculated as $d_i = R\cdot\sin\beta_i$, where R is the rotational radius and β_i denotes the angle between the axis of the i^{th} piston rod and AO. Here $\sin\beta_i$ can be calculated by Sine Law as:

$$\sin\beta_i = \frac{s\cdot\sin(\theta-\varphi_i)}{\sqrt{s^2+R^2-2s\cdot R\cos(\theta-\varphi_i)}}\,. \tag{2}$$

The torques generated by the cylinders are summed and applied at the crankshaft as:

$$\sum_{i=1}^{n}\tau_i = I_r\ddot{\theta} + \tau_o\,, \tag{3}$$

where I_r is the inertia of the rotational components, $\ddot{\theta}$ is the angular acceleration of output shaft and τ_o is the output torque. Thus, the correlation between the output torque and the forces provided by the cylinders can be described. Torque control is then made possible to be implemented on this actuator.

2) Dynamics modeling of hydraulic transmission

This section details the dynamics model of the rolling diaphragm-based hydraulic transmission, which describes the

relation between the input force F_{in} from the master side to the output force of F_{out} at the slave side. A spring-mass-damping system (**Fig. 3**) is adopted to approximate the interactions between the pistons and hydraulic fluid. Their interconnection is represented by the spring elements of stiffness $2K_t$, which account for the pipeline compliance and fluid compressibility. We assume that the system damping induced by the rolling diaphragm and fluid friction can be described by the coefficients *c* and B_f.

We first derive the pipeline compliance by considering that the input force F_{in} is applied at Piston 1 while the Piston 2 is blocked. The following equations in **(4)** describe the hoop stress σ_θ and radial stress σ_r at the inner pipe wall in response to the applied pressure *P*, according to Lamé Formula:

$$\sigma_\theta = P \cdot \frac{D_{pi}^2 + D_{po}^2}{D_{po}^2 - D_{pi}^2}, \sigma_r = -P, \tag{4}$$

where D_{po} and D_{pi} denote the outer and inner diameters of the pipeline. For pipes made of isotropic material with modulus of elasticity *E* and Poisson's ratio υ, the hoop strain is equivalent to $\varepsilon_\theta = \Delta D_{pi} / D_{pi} = (\sigma_\theta - \upsilon\sigma_r)/E$. The volume change in the pipe for an enclosed system should be equal to the change in the input cylinder, which gives $[(D_{pi} + \Delta D_{pi})^2 - D_{pi}^2]L_p = D_{in}^2 \cdot \Delta x_{in}$, where ΔD_{pi} is the change of pipe inner diameter, D_{in} is the diameter of input cylinder, Δx_{in} is the displacement of input piston and L_p is the length of pipe. Therefore, the inner diameter change of pipe could be determined by:

$$\Delta D_{pi} \approx D_{in}^2 \cdot \Delta x_{in} / (2 D_{pi} L_p). \tag{5}$$

With **(4)** to **(5)** and the assumption that the pressure comes from the input force $F_{in} = P \cdot (\pi D_{in}^2 / 4)$, the pipeline stiffness K_p observed at the piston can be derived as:

$$K_p = \frac{F_{in}}{\Delta x_{in}} = \frac{\pi E D_{in}^4}{8 D_{pi}^2 L_p} \left[\frac{D_{pi}^2 + D_{po}^2 + \upsilon D_{po}^2 - \upsilon D_{pi}^2}{D_{po}^2 - D_{pi}^2} \right]^{-1}. \tag{6}$$

The fluid stiffness due to compression could be modeled as $K_f = E_v \cdot A_{in}^2 / V$, where A_{in} is the cross-sectional area of the input cylinder, *V* is the total volume of fluid and E_v is the fluid bulk modulus. Hence, the equivalent transmission stiffness K_t of the hydraulic pipe can be calculated as the series of pipeline compliance and fluid stiffness: $K_t = K_p K_f / (K_p + K_f)$.

For the system damping factors, we assume that the input force at Piston 1 is F_{in} and it produces a movement at constant velocity, given that there is *zero* loading at the Piston 2 ($F_{out} = 0$). We can hence derive the fluid head loss, which is governed by the Bernoulli equation for steady and incompressible flow between any two points in a pipe:

$$\frac{P_{in}}{\rho} + \frac{v_{in}^2}{2} + g z_{in} = \frac{P_{out}}{\rho} + \frac{v_{out}^2}{2} + g z_{out} + h_f, \tag{7}$$

where P_{in} and P_{out} represent the fluid pressures, v_{in} and v_{out} are the fluid velocities, z_{in} and z_{out} represent the elevations, at the input and output piston respectively, h_f is the head loss ρ is the fluid density and *g* is the gravitational constant.

In this case, pipeline loss mainly contributes to head loss, while the local loss at the connections between cylinder and tube can be neglected. Because the pipeline loss is proportional to the length but *inversely* proportional to the diameters, the head loss in the cylinders is negligible when compared with that in the pipelines. The total pipeline loss can be approximated as $h_f = \lambda L_p v_f^2 / (2 D_{pi})$, where λ is the flow coefficient and v_f is the fluid velocity [22]. For laminar pipe flow, we can assume that $\lambda = 64 / R_e$, where the Reynolds number $R_e = \rho v_f D_{pi} / \mu$, and μ is the dynamic viscosity of fluid.

Assuming that the pipes are put at the same elevation, the terms gz_{in} and gz_{out} can be eliminated. The fluid is nearly incompressible so that the velocity at the input and output piston is approximately equal. The pressure P_{out} is zero in our case with no load ($F_{out} = 0$). By observing that $F_{in} = P_{in} \cdot A_{in}$, the equivalent damping coefficient B_f can be obtained as:

$$B_f = \frac{F_{in}}{v_{in}} = 8\pi\mu L_P \left(\frac{D_{in}}{D_{pi}} \right)^4. \tag{8}$$

For the fluid inertia, we consider an equivalent fluid mass as observed at the piston, which can be determined by an energy calculation $m_f v_{in}^2 = m_{cyl} v_{in}^2 + m_{pi} v_f^2$, where m_f is the equivalent mass of fluid, m_{cyl} is the fluid mass in cylinder, and m_{pi} is the fluid mass in the pipeline. Then the equivalent mass can be obtained as $m_f = m_{cyl} + m_{pi} (D_{in} / D_{pi})^4$.

The key components of the overall dynamics model of the passive fluid transmission system are shown in **Fig. 3**. The dynamics of the hydraulic transmission can be described by a linear differential equation as follows:

$$\mathbf{K}\mathbf{q} + \mathbf{C}\dot{\mathbf{q}} + \mathbf{M}\ddot{\mathbf{q}} = \mathbf{F}, \tag{9}$$

where

$$\begin{cases} \mathbf{K} = \begin{bmatrix} 2K_t & -2K_t & 0 \\ -2K_t & 4K_t & -2K_t \\ 0 & -2K_t & 2K_t \end{bmatrix} & \mathbf{C} = diag\left(c, B_f, c\right) \\ \mathbf{M} = diag(m_p, m_f, m_p) & \mathbf{F} = \begin{bmatrix} F_{in} & 0 & -F_{out} \end{bmatrix}^T \end{cases}. \tag{10}$$

In **(9)**, $\mathbf{q} = [q_1 \quad q_2 \quad q_3]^T$ denotes the matrix containing displacements of input piston (q_1), fluid (q_2) and output piston (q_3). Damping coefficient, *c*, is introduced by the rolling diaphragm. The state space function can be derived as:

$$\begin{bmatrix} \dot{\mathbf{q}} \\ \ddot{\mathbf{q}} \end{bmatrix} = \begin{bmatrix} 0 & \mathbf{I} \\ -\mathbf{M}^{-1}\mathbf{K} & -\mathbf{M}^{-1}\mathbf{C} \end{bmatrix} \begin{bmatrix} \mathbf{q} \\ \dot{\mathbf{q}} \end{bmatrix} + \begin{bmatrix} 0 \\ \mathbf{M}^{-1}\mathbf{F} \end{bmatrix}. \tag{11}$$

D. Design considerations

This section presents the design guidelines for the hydraulic system in regards to the desired system performance, namely fluid transmission stiffness and latency. Parametric study is performed by numerical simulation of the dynamics model. The study scope includes many form factors of the transmission

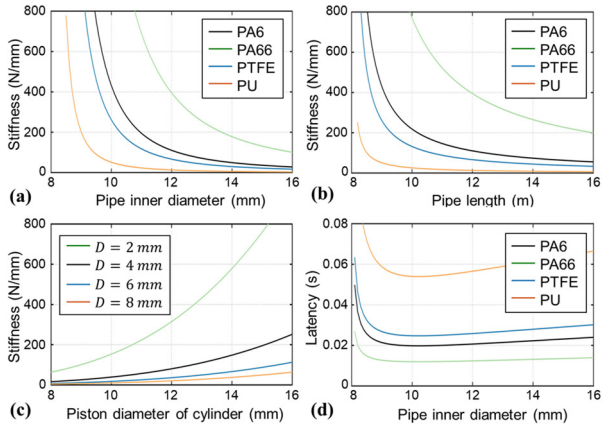

Fig. 4. Simulation showing the trend of transmission stiffness against: **(a)** pipe inner diameter; **(b)** pipe length; and **(c)** piston diameter. It can be observed that the stiffness profile is significantly affected by the pipe materials: PA 6, PA 66, PTFE and PU.

system, such as pipe diameter, length, thickness, materials, and cylinder diameter. *Four* typical pipe materials: polycaprolactam 6 (PA 6), PA 66, polytetrafluoroethylene (PTFE) and polyurethane (PU), are examined.

Transmission stiffness – The transmission stiffness has a compelling effect on the system repeatability and accuracy. **Fig. 4a-b** illustrate the trends of transmission stiffness under various pipe diameters and lengths. The stiffness decreases when the diameter or the length increases. It can also be observed that the choice of pipe material imposes a significant influence on the transmission stiffness. PA66 offers the highest transmission stiffness because it possesses the highest Young's modulus. However, the large bending stiffness of PA66 (0.17 N-m^2 with outer/inner diameter of Ø6/4 mm) hinder its application in conditions that requires flexible arrangement. **Fig. 4c** shows that the enlargement of piston diameter could also enhance the transmission stiffness, due to the increased piston diameter to pipe inner diameter ratio.

Transmission latency – The power transmission in this system could be considered as the simultaneous occurrence of pressure and velocity changes. Such velocity of pressure transient through fluid in a closed conduit could be deduced as:

$$c_p = \left(\sqrt{\frac{\rho \psi D_{pi}}{T_p \cdot E} + \frac{\rho}{E_v}} \right)^{-1}, \qquad (12)$$

where the parameters are summarized in **Table I** [23]. The pipe support factor ψ is a function of the pipe material (υ), the pipe inner diameter (D_{pi}) and the pipe wall thickness (T_p), which can be calculated as following for the case of thick-walled pipe ($D_{pi}/T_p < 10$) without anchorage throughout the length [23]: $\psi = 2e(1+\upsilon)/D_{pi} + D_{pi}/(D_{pi}+T_p)$.

Fig. 4d shows that the latency with baseline parameter values is around 21 ms (with the ratio of pipe inner diameter to thickness varying and pipe thickness fixed at 1 mm). The enlargement of pipe inner diameter over 2 mm causes a slight increase of the latency. But the decline of the diameter under 1 mm will bring the significant rise in latency. Meanwhile, the latency is also proportional to the pipe length. And more rigid pipe material will reduce the transmission latency.

TABLE I PHYSICAL PARAMETERS

Parameter	Description	Parameter	Description
c_p	Velocity of pressure transient in fluid	υ	Poisson's ratio of pipe material
E_v	Bulk modulus of fluid	D_{pi}	Pipe inner diameter
E	Young's modulus of pipe material	e	Pipe wall thickness
ρ	Fluid density	ψ	Pipe support factor

Overall, several design tradeoffs are developed to account for the required dynamics performance and dedicated operating conditions. Shorter pipelines are preferable as a general design rule to reduce the fluid inertia, give rise to a higher transmission stiffness, and decrease the transmission latency. For surgical applications that emphasize positional accuracy, such as breast or prostate biopsy, pipelines with a smaller diameter and pistons with a larger diameter should be adopted to enhance the transmission stiffness. However, a small pipe diameter (< 2mm) will dramatically increase transmission latency and damping, which will deteriorate the control and stability. Therefore, the pipeline diameter shall be expanded to accommodate for applications that require a rapid dynamic response, such as tele-manipulation of a catheter in a master-slave manner.

III. EXPERIMENTAL RESULTS

We have conducted several experiments to evaluate key performance indices of the proposed hydraulic transmission, including step response, force dynamic transmission, positional frequency response and sinusoidal positional tracking. In all these experiments, master and slave components of the transmission were connected by 10-meter semi-rigid nylon (PA 6) tubes, which had inner and outer diameters of ID:Ø4 mm and OD:Ø6 mm, respectively. We choose distilled water as the hydraulic fluid, accrediting to its availability and ease of implementation. The water pressure pre-loading in all pipelines was controlled by a pressurized air supply system, a pressure regulating valve and a fluid reservoir. Not only could this eliminate backlash, but it could also ensure the symmetric folding/unfolding of rolling diaphragms, thus reducing friction during fast motion transmission.

A. Step response of the single-cylinder actuation

Step response experiments were conducted to evaluate the force transmission behavior in a pipeline with both ends of cylinders (**Fig. 2**). At the master side, a DC motor (HFmotor-40150, Chengdu Hangfa Hydraulic Engineering Co., Ltd) actuated the master cylinder through the rack-and-pinion mechanism, which transmitted torque to linear force. The output force at slave cylinder was measured by a force sensor (MIK-LCS1, Hangzhou Meacon Automation Technology Co., Ltd) embedded on the piston rod. Water in the pipelines was preloaded at 0.05 MPa to ensure the mechanical couplings were fully engaged, which corresponded to 5 N force output on the slave cylinder at the initial state. Two step inputs, i.e. 26 N and 78 N, were applied to the master cylinder. The corresponding measured force responses are shown in **Fig. 5**. Simulated results deduced by the dynamics model in **Section II.D** are also overlaid, predicting a similar response to the measured results. The response time is within 40 ms from the signal input and the

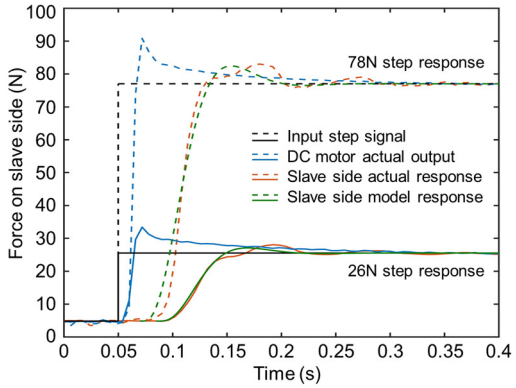

Fig. 5. Step response of a single cylinder transmission, which were measured in two different steps of magnitudes. Experimental and modeled responses are compared. The response time from the signal input is within 40 ms.

10%-to-90% rise time is 25 ms for both step input forces. This rise time remains constant for different input forces, depicting an important feature for a linear time-invariant system. The settling time with 5% error band is about 0.17 s, indicating that the proposed hydraulic transmission can rapidly transmit the force, even via a 10-meter long pipeline. These characteristics are crucial to the highly responsive force transmission required in many typical teleoperated robot systems.

B. Force transmission performance

Force transmission performance of the three-cylinder continuous motor (**Fig. 1**) was evaluated in a weight-lifting experiment, in which three master cylinders were individually actuated by electric motors through leadscrew drives. The output shaft was coupled to a winch of diameter Ø40 mm. With the hydraulic fluid pre-loaded at 0.1 MPa, the master-slave actuator can lift 2.5 kg at a constant velocity of 50.24 mm/s, corresponding to an output torque of 0.49 N·m and a net power of 1.23 W. The volumetric power density of the hydraulic transmission is 2.46 kW/m^3. The torque/power outputs of this motor are mainly determined by the electric motor inputs at the master side. In principle, the continuous motor can generate power as much as the electric motors can afford, until the weakest component with lower strength limit fails, e.g. tiny gear teeth and thin rolling diaphragms.

C. Positional frequency response

The dynamic performance of a three-cylinder continuous actuator (**Fig. 1**) was investigated with a frequency response method. No loading was added to the slave actuator. The three master cylinders were controlled based on the inverse kinematics derived in **Section II.C**. The slave actuator could thus follow the periodic sinusoidal input of master actuator under open-loop control, where the angular position $\theta = A\sin(\omega \cdot t)$. The amplitude was 5° and the test frequency was from 0.1 Hz to 7 Hz. The output angular position was measured by a differential encoder coupled with the output shaft.

Fig. 6 illustrates the Bode plots of magnitude M and the phase-shift ξ of the continuous actuator at steady state. Note that for a linear time-invariant system, the frequency response at steady state becomes $\tau_{ss} = M \cdot A\sin(\omega \cdot t + \xi)$. The magnitude plot indicates that the magnification increases with the preloaded fluid pressure. The magnification value peaks at

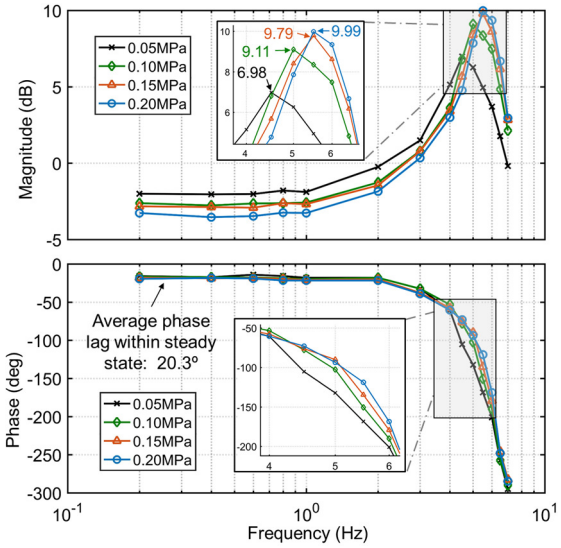

Fig. 6. Experimental frequency response of the three-cylinder actuation at four levels of hydraulic pressure. The input is positional signal of electric motor (master), and the output is the encoded position of our motor (slave).

around 5 Hz, which corresponds to the natural frequency of the overall hydraulic transmission. The phase lag of the transmission is kept at around 20.3° for low actuation frequency (≤ 2 Hz). It is also found that the increase of the preloaded fluid pressure does not significantly affect the natural frequency and phase lag. The transmission with preloaded fluid pressure 0.2 MPa had small time delay: only 60 ms and 52 ms at actuation frequency 1 Hz and 5 Hz, respectively.

D. Sinusoidal positional tracking

To evaluate the accuracy of the 3-cylinder actuator under open-loop control, a positional tracking test was performed. The setup was the same as described in **Section III.C**, but the periodic sinusoidal input at the master side is less frequent, once per 20 s (0.05 Hz), covering a larger motion range of 360°. This sinusoidal tracking performance is illustrated in **Fig. 7**, which shows the input and output angular motion profile overlaid, as well as the corresponding error in angular displacement. It also demonstrates that the 3-cylinder continuous actuator can track the positional input over the range of 360°. The average error between the input and output within one cycle is 0.64°, ensuring the proposed actuator can be

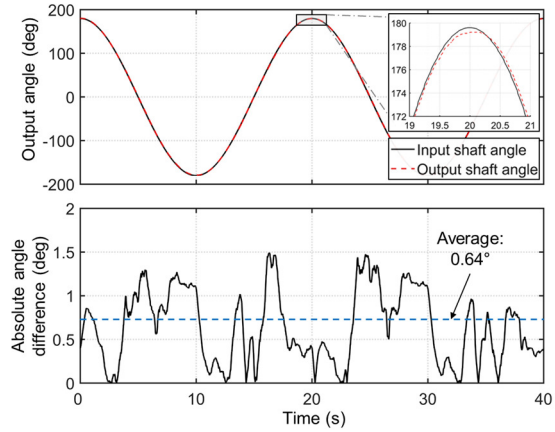

Fig. 7. Sinusoidal tracking of angular displacement during the three-cylinder actuation throughout two cycles in 40 s. Precise feed-forward control is observed, with an average absolute error of 0.64°.

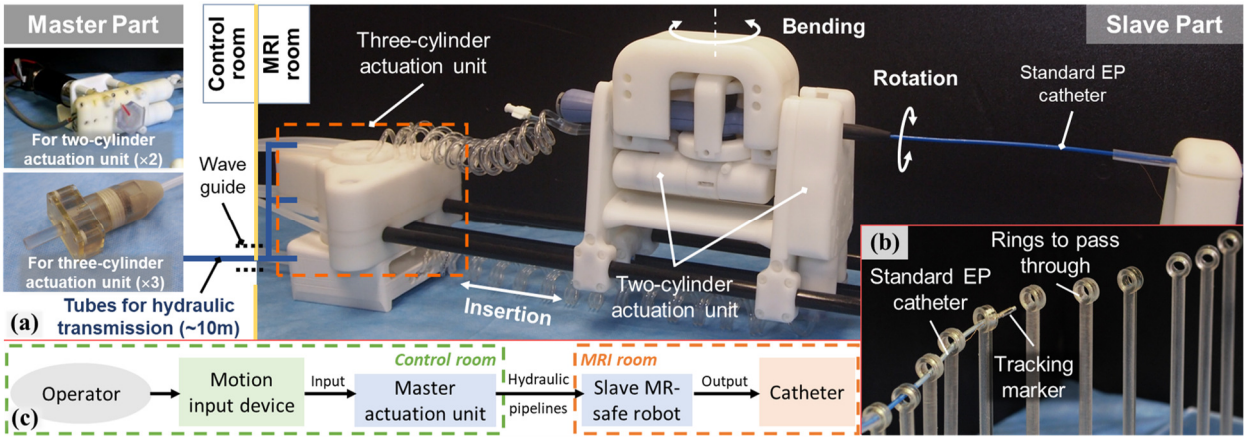

Fig. 8. MR safe robot prototype incorporating 3 sets of hydraulic transmission units for 3-DoF manipulation of a standard EP catheter. A three-cylinder unit pushes/pulls the catheter precisely in long-range navigation. Master-slave motion is transmitted from control to MRI room through a pair of 10-meter long pipelines. **(b)** EP ablation catheter tele-manipulated to pass through a series of 11 rings. The 3-D position of catheter tip is EM-tracked for our validation; **(c)** Block diagram illustrating the architecture of the robotic catheter system.

manipulated by open-loop control accurately.

In summary, the master-slave actuator has fast step response (< 40 ms), high payload (0.49 N·m), quick frequency response (60 ms at 1 Hz and 0.2 MPa), and precise feed-forward control (ave. error of 0.64°). The performance in step response (**Fig. 5**) and frequency response (Bode plot, **Fig. 6**) have demonstrated the sufficiently low latency of force/position transfer within the range of 0.1-2 Hz. Compared with the previous two-cylinder actuator presented in [19], the key improvement of the new three-cylinder hydraulic motor is to provide continuous bidirectional actuation with unlimited motion range. In addition, it can achieve a significant improvement in accuracy to 0.64°/1.50° (avg./max.), while the accuracy of previous actuator is 1.46°/2.56° (avg./max.). It can be attributed to our the reduced friction in the new three-cylinder crank shaft design, without using any plastic gear. The frequency response remains similar due to the unchanged hydraulic pipeline parameters (e.g. diameter, length, material, transmission fluid).

IV. MR Safe Robot for Cardiac Catheterization

The proposed three-cylinder hydraulic motor is incorporated into an MRI-guided robotic catheter platform [19, 24] (**Fig. 8a**). This aims to improve the catheter insertion/reciprocating motion. Not only does it enable long range catheter advancement (340 mm) in the human body, but it also allows rapid push/pull of catheter with high fidelity. This feature is crucial for delicate EP tasks, such as electro-anatomic mapping (EAM) and radiofrequency (RF) ablation for cardiac EP. The steering and rotation of catheter are achieved by our previous two-cylinder actuators with a motion range of ±45° and ±360° respectively. An EP catheter (Thermocool® Bi-Directional Catheter, Biosense Webster Inc.) can be readily integrated to the robot, providing full range tip steering of ±180°.

To evaluate this tele-operated robotic catheterization, an experiment was conducted to simulate the long-range navigations, such as from femoral vein to heart chamber. *Eleven* rings (ID=Ø7 mm) were placed serially along 310-mm distance with an average spacing of 31 mm (**Fig. 8b**). The detailed dimensions are stated in **Fig. 9a**. A smooth curve linking the ring centers in series simulates a path along the vessel to heart chamber (**Fig. 9b**). This task would be found more difficult relative to the navigation in human vein (ID≈Ø9.4 mm) and inferior vena cava (ID≈Ø20 mm) [25, 26].

During the task, a standard EP catheter with an outer diameter of 8 Fr (≈Ø2.7 mm) is manipulated by the robot that is tele-controlled by a 3D motion input device (Novint Falcon, NF1-L01-004). To record the position and orientation (pose) of the catheter, a 6-DoF EM positional sensor (Ø0.8×9 mm, NDI

(a) Details of the experiment

Experimental settings	
No. of rings	11
Inner diameter of the rings (mm)	7.0
Dimension of the setup (L×W×H mm)	310× 70×32
Avg. spacing of rings along *x*-axis (mm)	31.0
Robot performance	
Total time (s)	96.0
Average time interval per ring (s)	9.6
Min./max. interval between two adjacent rings (s)	1.9/ 19.8
Avg./max. value of deviation (mm)	3.03/ 9.25

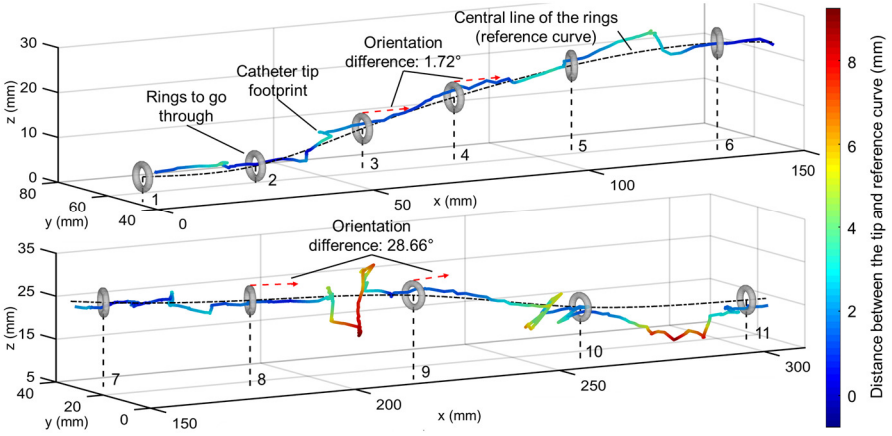

Fig. 9. **(a)** Key parameters of the experimental setup and the catheterization performance indices; **(b)** Actual footprint of the catheter tip compared with the reference curve along the series of rings of 1st–6th (Upper) and 7th–11th (Lower). The more the catheter tip deviated from the reference curve, warmer the color of its tip footprint. A large difference in the orientation of two adjunctive rings, e.g. from the 8th to the 9th, makes the navigation challenging.

Medical Aurora), with a tracking accuracy of 0.48mm, is attached near the catheter tip (**Fig. 8b**). A subject, who learned the robot control in advance, was invited to perform the task. The subject could look at the catheter tip, and adjust the manipulation so as to pass through the rings. **Fig. 8c** illustrates the system architecture of the robotic catheter system.

The diagrams in **Fig. 9b** depict the catheter tip footprint along the series of 11 rings. The deviation from the tip to the reference curve is indicated by the warm color gradient. A mean value of deviation, 3.03 mm, was found throughout the entire trajectory. Most sections of navigation are smooth and closed along with the reference curve. But several sections of the tip footprint involve more deviations, particular when the orientation difference of adjacent rings is relatively large.

V. Conclusion

We present a design of an MR safe hydraulic motor that incorporates three rolling-diaphragm-sealed cylinders. Mechanical power can be transferred through the passive hydrostatic transmission along the long hydraulic tubes. Unlike the two-cylinder motor design, the presented motor can provide continuous bidirectional rotation with unlimited range. It also features fast response (rise time < 40 ms), precise open-loop control of position (averag error of 0.64°) and high output torque (0.49 N·m) through 10-meter long hydraulic pipelines. Currently, there is no such kind of MR safe hydraulic master-slave follower. Both kinematics and dynamics models of the motor have also been devised to identify the key design parameters that govern the system performance, namely transmission stiffness and latency. Their design tradeoff is also presented in an analytical study.

To further evaluate the practical value of our motor, we have integrated it into an MRI-guided catheter robot for cardiac EP. This shows its capacity to perform high-fidelity tele-manipulation of the standard EP catheter, and also its potential in other types of interventions demanding for intra-op MRI guidance, such as breast, prostate biopsy, stereotactic neurosurgery [27]. This robot-assisted approach would add much confidence to surgeons with sufficient MR-based guidance revealed on multiple displays in the control room.

We also foresee that MRI-guided HIFU thermal therapy is another emerging intervention that could benefit from the present motor. The high-payload, continuous actuation would facilitate accurate repositioning of the large array of ultrasound transducers, hence enlarging the ablation workspace, and also smoothening the interventional workflow without having to going in-and-out the MRI room for manual repositioning.

References

[1] T. Kahn and H. Busse, *Interventional magnetic resonance imaging*. Springer, 2012.

[2] S.-E. Song *et al.*, "Development of a pneumatic robot for MRI-guided transperineal prostate biopsy and brachytherapy: New approaches," in *IEEE International Conference on Robotics and Automation* 2010, pp. 2580-2585, 2010.

[3] G. Rahmathulla, P. F. Recinos, K. Kamian, A. M. Mohammadi, M. S. Ahluwalia, and G. H. Barnett, "MRI-guided laser interstitial thermal therapy in neuro-oncology: a review of its current clinical applications," *Oncology,* vol. 87, no. 2, pp. 67-82, 2014.

[4] J. Fritz, C. Thomas, S. Clasen, C. D. Claussen, J. S. Lewin, and P. L. Pereira, "Freehand real-time MRI-guided lumbar spinal injection procedures at 1.5 T: feasibility, accuracy, and safety," *American Journal of Roentgenology,* vol. 192, no. 4, pp. W161-W167, 2009.

[5] A. Tzifa *et al.*, "Magnetic Resonance–Guided Cardiac Interventions Using Magnetic Resonance–Compatible Devices," *Circulation: Cardiovascular Interventions,* vol. 3, no. 6, pp. 585-592, 2010.

[6] Y. Feng *et al.*, "An efficient cardiac mapping strategy for radiofrequency catheter ablation with active learning," *International Journal of Computer Assisted Radiology and Surgery,* pp. 1-9, 2017.

[7] K. Masamune *et al.*, "Development of an MRI-compatible needle insertion manipulator for stereotactic neurosurgery," *Journal of Image Guided Surgery,* vol. 1, no. 4, pp. 242-248, 1995.

[8] A. N. Sridhar *et al.*, "Image-guided robotic interventions for prostate cancer," *Nature reviews Urology,* vol. 10, no. 8, pp. 452-462, 2013.

[9] K. Chinzei, N. Hata, F. A. Jolesz, and R. Kikinis, "MR compatible surgical assist robot: System integration and preliminary feasibility study," in *MICCAI*, 2000, vol. 1935, pp. 921-933, 2000.

[10] H. Su *et al.*, "A MRI-guided concentric tube continuum robot with piezoelectric actuation: a feasibility study," in *IEEE International Conference on Robotics and Automation*, 2012, pp. 1939-1945, 2012.

[11] Y. Chen, K. W. Kwok, and Z. T. H. Tse, "An MR-conditional high-torque pneumatic stepper motor for MRI-guided and robot-assisted intervention," *Annals of biomedical engineering,* vol. 42, no. 9, pp. 1823-1833, 2014.

[12] D. B. Comber, J. E. Slightam, V. R. Gervasi, J. S. Neimat, and E. J. Barth, "Design, additive manufacture, and control of a pneumatic mr-compatible needle driver," *IEEE Transactions on Robotics,* vol. 32, no. 1, pp. 138-149, 2016.

[13] Z. Guo, T. T. L. Lun, Y. Chen, H. Su, D. T. M. Chan, and K. W. Kwok, "Novel design of an MR-safe pneumatic stepper motor for MRI-guided robotic interventions," in *Proceedings of The Hamlyn Symposium on Medical Robotics*, 2016.

[14] D. Stoianovici *et al.*, "MR safe robot, FDA clearance, safety and feasibility of prostate biopsy clinical trial," *IEEE/ASME Transactions on Mechatronics,* vol. 22, no. 1, pp. 115-126, 2017.

[15] V. Groenhuis, J. Veltman, F. J. Siepel, and S. Stramigioli, "Stormram 3," *IEEE Robotics & Automation Magazine,* vol. 1070, no. 9932/17, 2017.

[16] G. Ganesh, R. Gassert, E. Burdet, and H. Bleuler, "Dynamics and control of an MRI compatible master-slave system with hydrostatic transmission," in *IEEE International Conference on Robotics and Automation* 2004, vol. 2, pp. 1288-1294, 2004.

[17] L. Lindenroth *et al.*, "Stiffness-based modelling of a hydraulically-actuated soft robotics manipulator," in *IEEE/RSJ International Conference on Intelligent Robots and Systems*, 2016, pp. 2458-2463, 2016.

[18] J. P. Whitney, T. Chen, J. Mars, and J. K. Hodgins, "A hybrid hydrostatic transmission and human-safe haptic telepresence robot," in *IEEE International Conference on Robotics and Automation*, 2016, pp. 690-695, 2016.

[19] K. H. Lee *et al.*, "MR Safe Robotic Manipulator for MRI-guided Intra-cardiac Catheterization," *IEEE/ASME Transactions on Mechatronics,* vol. 23, no. 2, pp. 586-595, 2018.

[20] T. Helbich *et al.*, "Evaluation of needle size for breast biopsy: comparison of 14-, 16-, and 18-gauge biopsy needles," *AJR. American journal of roentgenology,* vol. 171, no. 1, pp. 59-63, 1998.

[21] D. Stoianovici, A. Patriciu, D. Petrisor, D. Mazilu, and L. Kavoussi, "A new type of motor: pneumatic step motor," *IEEE/ASME Transactions On Mechatronics,* vol. 12, no. 1, pp. 98-106, 2007.

[22] R. W. Fox, A. T. McDonald, and P. J. Pritchard, *Introduction to fluid mechanics*. New York: John Wiley & Sons 1998.

[23] D. A. Thorley, *Fluid transients in pipeline systems*. ASME Press, 2004.

[24] K. W. Kwok, Z. Dong, Z. Guo, D. K. C. Fu, K. H. Lee, and C. L. Cheung, "Robotic catheter system for mri-guided cardiovascular interventions," Patent US15/630,406; PCT/CN2017/089701, 2017.

[25] J. Mortensen, S. Talbot, and J. A. Burkart, "Cross-sectional internal diameters of human cervical and femoral blood vessels: Relationship to subject's sex, age, body size," *The Anatomical Record,* vol. 226, no. 1, pp. 115-124, 1990.

[26] M. Prince, R. Novelline, C. Athanasoulis, and M. Simon, "The diameter of the inferior vena cava and its implications for the use of vena caval filters," *Radiology,* vol. 149, no. 3, pp. 687-689, 1983.

[27] Z. Guo *et al.*, "Compact Design of a Hydraulic Driving Robot for Intra-operative MRI-guided Bilateral Stereotactic Neurosurgery," *IEEE Robotics and Automation Letters,* vol. 3, no. 3, pp. 2515 - 2522, 2018.